Contents lists available at ScienceDirect

Chemical Engineering Research and Design

journal homepage: www.elsevier.com/locate/cherd

Experimental determination and computational prediction of the mixing efficiency of a simple, continuous, serpentine-channel microdevice

Siril Arockiam [a], *Yu Hsuan Cheng* [a], *Piero M. Armenante* [a,**], *Sagnik Basuray* [a,b,*]

[a] *Department of Chemical and Materials Engineering, New Jersey Institute of Technology, Newark, NJ, 07102, USA*
[b] *Department of Biomedical Engineering, New Jersey Institute of Technology, Newark, NJ, 07102, USA*

ARTICLE INFO

Article history:
Received 29 October 2019
Received in revised form 23 December 2020
Accepted 22 January 2021
Available online 1 February 2021

Keywords:
Computational Fluid Dynamics or CFD
Microfluidics
Mixing
Xurography
Serpentine channel
Simulation

ABSTRACT

Micromixing devices often utilize complex architectures to mix miscible liquid streams and can be complex and expensive to fabricate. Here, we developed, built, experimentally tested, and computationally analyzed a serpentine micromixer that can be fabricated using simple tools and supplies available in non-microdevice dedicated laboratories. Fluorescence imaging was used to quantify its mixing effectiveness experimentally. A Computational Fluid Dynamics (CFD) software package (COMSOL) was used to model the micromixing process. The predictions were in excellent agreement with the experimental data. The serpentine micromixer can achieve significant levels of mixing efficiency. CFD predictions for a straight microfluidic channel of the same length as the serpentine favorably compared with previous theoretical predictions, indicating that the serpentine's mixing efficiency was vastly superior. Finally, CFD predictions were conducted for different and possibly improved designs of the basic serpentine. In all cases, the mixing efficiency was primarily associated with the number of 90o elbows in the device rather than the straight sections' length, with the first serpentine bend playing a significant role. Future design improvements should focus on incorporating as many elbows as possible in the device to maximize mixing efficiency and reduce the device size.

1. Introduction

Microfluidics, the handling, manipulation, and control of fluids at the sub-millimeter scale are typically associated with processing fluids through a small channel having dimensions of tens or hundreds of micrometers (Lin, 2011). Microfluidic devices offer several attractive features since they are intrinsically small, compact, and portable. Many of the microfluidic applications found in the literature involve chemical analysis, providing useful capabilities such as the ability to process tiny quantities of samples and reagents to carry out detection with high resolution and sensitivity (Cheng, 2019; Zhenglong, 2019). Microfluidics offers the additional advantage of an increased surface-area-to-volume ratio in these applications, thereby reducing the reagent or sample consumption and increasing surface reactions.

One of the critical components of microfluidic devices is the microfluidic mixer, whose function is to provide adequate mixing to two or more incoming microfluidic streams. Microfluidic mixers, or micromixers, find application in many biochemical processes such as the synthesis or sequencing of nucleic acids (Cheng, 2019), DNA purification (Fan et al., 2013), chemical reactions (Cheng, 2020), and polymerase chain reactions (Capretto et al., 2011). Microfluidic mixers offer the additional advantage of reducing reaction time, such

* *Corresponding author at*: Department of Chemical and Materials Engineering, New Jersey Institute of Technology, Newark, NJ, 07102, USA.
** *Corresponding author*.
E-mail addresses: piero.armenante@njit.edu (P.M. Armenante), sbasuray@njit.edu (S. Basuray).

https://doi.org/10.1016/j.cherd.2021.01.022

as decreasing the incubation time for bead-based enzyme-linked immunosorbent assays (ELISA) (Verma et al., 2018).

However, one of the most significant disadvantages of microfluidic mixers is the fluid's laminar flow profile in the microfluidic mixers. Because of the small channel dimension, the Reynolds Number in micromixers is typically low, i.e., on the order of 0.1 to 0.01 in a typical water-based microfluidic system (Buchegger et al., 2011). Because of the absence of turbulence at such low Reynolds numbers, the dominant mixing mechanism is the molecular diffusion of the mixing species. Since diffusion is an inherently slow process even at this scale, mixing efficiency in microfluidic channels has been augmented using active (through external forces) or passive (via intelligent channel design) methods. Active micromixing is often achieved by integrating into the micromixers devices such as mechanical ultrasonic transducers (Ahmed et al., 2009; Luong et al., 2011), thermal actuators (Xu et al., 2010), periodic electro-osmotic flow generators (Lim et al., 2010), magnetohydrodynamic flow generators (Wang et al., 2008), and dielectrophoretic transducers (Campisi et al., 2009). However, incorporating active mixing in microfluidics requires external devices, complex fabrication, heat generation, and significant power requirements. As a result, there has been significant interest in the development of passive mixers.

In passive micromixing devices, a significant increase in mixing efficiency is achieved by increasing the contact area between the mixing species using simple 2D channels or more complex 3D architectures. Ortega-Casanova and Lai, as well Lee et al., showed that 3D micromixers promote chaotic mixing, allowing for a significant increase in the mixing efficiency (Lee et al., 2016; Ortega-Casanova and Lai, 2018). Many 3D passive mixers utilize multiple splitting, recombining, or rotating channels, incorporating structures with twists (Zhang et al., 2012), as well as embedded barriers (Park et al., 2009), staggered herringbone (Du et al., 2010), or Tesla structures (Hossain et al., 2010; Yang et al., 2015) to increase the mixing efficiency. Ansari and Kim (2010), Ansari et al. (2010) and Chung et al. (2010) have shown that multiple intersecting channels can enhance the mixing performance by continuously spitting and rearranging the flow (in so-called "SAR" devices), typically resulting in the formation of Dean vortices and enhanced flow circulation. Afzal and Kim (2012, 2015) and Parsa et al. (2014) have shown that repeated splitting and recombining microchannels can achieve a significant increase in mixing performance due to induced secondary flows in the subchannels. Other researchers have constructed embedded barriers (Park et al., 2009), expansion chambers, and inter-connected fluid networks to further increase the chaotic advection or sustain the Dean vortices. Du et al. (2010) and Tóth et al. (2014), as well as other investigators, have shown that a staggering herringbone micromixer (SHM) could significantly increase the mixing efficiency by sustaining two transverse vortices whose orientations strictly depend on the structural asymmetry. Recently, other research groups have incorporated Tesla structures (Hossain et al., 2010; Yang et al., 2015) to achieve similar mixing efficiency.

Other investigators, like Ortega-Casanova and Lai and others, have shown that simple serpentine-type microdevices can be effectively used to achieve significant mixing efficiency without the additional requirements of more complex designs (Ortega-Casanova, 2016, 2017a, 2017b; Ortega-Casanova and Benitez-Alcaide, 2017; Ortega-Casanova and Lai, 2018; Salas and Ortega-Casanova, 2016). For example, Buchegger et al. (2011) proposed a multi-lamination serpentine micromixer based on wedge-shaped inlet channels. Their experimental results revealed highly uniform fluid mixing in the low millisecond-second range. Ammar et al. (2014) showed that T-intersections at the inlets have higher mixing efficiency than Y-intersections due to the significant increase in the interfacial mass driving forces. Recently, Chen et al. (2016) have shown that a square wave serpentine micromixer's mixing efficiency was superior to that of a zigzag channel micromixer or other types of serpentine micromixers.

Most of the 3D passive micromixers mentioned above require extensive fabrication, multiple soft lithographic steps, complex, time-consuming assembly, limiting their usage. Bartholomeusz et al. and Treise et al. did preliminary work for an innovative microfabrication technique called Xurography, a technique based on thin, pressure-sensitive double-sided adhesive flexible films and a cutter plotter (Bartholomeusz et al., 2005; Treise et al., 2005). This technique involves removing materials, following the desired pattern, from thin-film through a cutting blade controlled by cutter plotters used originally for fabric design and advertisement purposes (Islam et al., 2015). The design can be accomplished using basic CAD tools for Xurography, and the production of the design takes a few minutes.

This review shows that micromixers can be complex and expensive to fabricate. In this work, we propose using a micromixer that can be simply and inexpensively built, making microfluidic mixers straightforward in their fabrication, economical, and readily available in most laboratories without the need for highly skilled personnel, extensive training, and dedicated and costly fabrication equipment. We developed, built, experimentally tested, and computationally analyzed a serpentine micromixer obtained by using simple tools and supplies available in non-microdevice dedicated laboratories to achieve this goal. We used widely available double-sided, adhesive films to obtain serpentine microchannels of desired depth using a commercially available, inexpensive cutting machine, and properly assembled them with other simple components to fabricate highly effective micromixers.

The method proposed in our work to make serpentine channels for micromixing purposes can offer tremendous versatility to microfluidics researchers, including the possibility of using similar or even more complex microdevices with different fluids for advanced analytical sensing of biological molecules and chemical moieties or as electrocatalysts. This approach could help researchers overcome many problems faced during sensor device development, including inactivation of biological capture molecules, long-term packing, sensitivity, and selectivity. More in general, the ability to manufacture these micromixers has the advantage of making microfluidic mixers straightforward in their manufacturing, inexpensive, and readily available in most laboratories without the need for dedicated personnel, extensive training, multiple fabrication steps, complex and costly fabrication equipment, and tedious assembly processes.

Previous researchers have often overlooked the computational and theoretical validation of the mixing characteristics and efficiency of 3D passive micromixers. Here we were not only interested in building and experimentally testing micromixing devices but also in numerically simulating their mixing characteristics and validating the numerical predictions against experimental data to quantify their robustness. In this work, we conducted Computational Fluid Dynamic (CFD) numerical simulations to determine how reliably this approach was to predict our experimental results in a serpentine channel, as well as to investigate the mixing performance behavior of different channel architectures without the need for additional experimental verification.

In this work, mixing experiments were conducted using a microfluidic mixing channel rapidly built by cutting a polyester double-sided adhesive tape with an inexpensive cutting machine (below US $200) and applying it to glass slides. This approach ensured that other research groups could easily replicate our microfluidic channels without a significant increase in personnel or additional costs. Fluorescence imaging was performed to quantify the mixing efficiency of this device using aqueous solutions. Commercially available Computational Fluid Dynamics (CFD) modeling software (COMSOL) was used to implement a 3D CFD model of the same devices to validate the computational approach (and thus the appropriateness of its use for similar systems in the absence of additional experimentation) and to corroborate the experimental results. CFD modeling for a straight microfluidic channel was conducted to quantify the intensification in mixing efficiency produced by the serpentine design compared to a straight channel of the same length and cross-sectional area. These computational results were also compared with previous theoretical predictions for straight channels (Lam et al., 2005). Finally, having validated the CFD predictions, we used the same computational approach to explore the performance of modified architectures, including those with as different depths of the channels, length of the straight sections of the serpentine design, channel entry geometries (T-channel and Y-channel inputs), and flow rates, which could result in improved mixing efficiency. This approach was found to be very useful to better understand each design parameter's role in mixing efficiency and especially the critical role of the bends in the serpentine channel, which were the significant contributors to improving mixing effectiveness.

2. Experimental apparatus, materials, and methods

2.1. Device design and fabrication

The microfluidic device built and used in this work, and shown in Fig. 1, consisted of three layers, i.e., (1) a top glass slide with drilled holes for solvent input and output, (2) a bottom glass slide, and (3) a microfluidic mixing channel cut from a double-sided polymer-based adhesive tape (Arcare® 90445) (Huang et al., 2016) sandwiched between the two glass slides. This tape was a transparent, thin, flexible acrylic polyester film coated on both sides with a medical-grade pressure-sensitive adhesive (AS-110; Adhesive Research Inc.) (Nath et al., 2014). The tape was protected initially on both sides by the top and bottom liners, which were removed during the device assembly process. The polyester film thickness was 25 μm, and the thickness of each of the two adhesive layers was 28 μm, thus bringing the total thickness of the channel to 81 μm. The top and bottom glass slides (25 mm × 75 mm × 1 mm), had ground edges and 90° corners (Globe Scientific Inc). The top glass slide was drilled using a 1-mm diamond drill bit to obtain two inlets and one outlet. The glass slides were cleaned with well-established AMD cleaning protocols to remove organic and inorganic residues from the glass surface (Lake et al., 2015).

The desired serpentine pattern (Fig. 1A and B) was cut into the tape using a widely available commercial die-cutting machine to cut paper, felt, vinyl, and fabric (Cricut Explore® electronic cutting machine). A carbide stainless-steel blade was used to cut the desired design pattern. The first step in fabricating a 2D serpentine channel consisted of designing the channel shape using Cricut® software. The vinyl-cutting setting for the cutting machine was then selected to cut the desired two-dimensional (2D) serpentine channel pattern in the polyester-based adhesive tape (with the removable liners still attached). The serpentine cut into the tape consisted of 13 straight sections, each 7.5 mm-long, connected at 90°, with further inlet and outlet sections (Fig. 1D). The serpentine channel had a total overall length of 112 mm (L), a 700 μm width (W), and the same depth (D) as the polyester film plus the two adhesive layers (81 μm) once the liners were removed. The device had a total final channel volume of 6.35 μL.

The microfluidic device was assembled by removing the tape liner on one side of the plastic tape, carefully aligning the tape along the glass slide's edges, and then affixing it onto the glass slide surface. The tape was pressed hard on the glass slide to ensure that no air bubbles were left between the glass slide and the adhesive tape. The last step consists of removing the top liner from the tape (already mounted on the bottom glass slide), aligning the microfluidic channel with inlet and outlet openings on the top glass slide, and pressing the top glass slide. Repeated microscopic observations were made to ensure that no air bubbles were present. Prefabricated plastic fluid ports (McMaster-Carr) were glued to the inlet and outlet openings using a commercially available acrylic glue and left to dry undisturbed for 15 min. Post assembly, the serpentine channel was qualitatively visually inspected for integrity and proper operation by feeding it with solutions of red and green food colorants (Fig. 1C).

2.2. Experimental method

The two inlet openings in the microdevice (Inlets 1 and 2) were connected with Tygon S3 flexible tubing (Saint-Gobain, USA) to two 3 mL syringes (BD, USA) with an inner diameter of 8.42 mm. The syringes were inserted in New Era NE-1000 programmable single-channel syringe pumps (New Era Pump Systems Inc.) to feed the desired solutions at the desired controlled flow rates. The first channel was fed with distilled water, while the second channel was fed a 1-mM Fluorescein Isothiocyanate (FITC) solution prepared by dissolving 3.89 mg FITC (Sigma Aldrich®) in 10 mL of distilled water (Millipore Sigma).

The assembled microfluidic device was observed using an Olympus BX51TF fluorescence microscope with an Abbe Condenser, 50.8 mm × 7.63 mm (2 in. × 3 in.) Mechanical Stage, 4X U PlanFl Objectives, DAPI/FITC/TRITC filter cubes, and a 100 W Mercury Lamp source. The microscope was additionally provided with a 0.63X C-mounted, 100 frames/s ORCA-Flash4.0 V2 Digital CMOS Hamamatsu camera C11440-22CU to capture images.

The desired flow rate was programmed into the syringe pumps. It was ensured that the flow rates were identical at both inlets and that the pumps were started simultaneously. Experiments were conducted using two values of the overall flow rate, Q, i.e., 0.1 μL/min, and 10 μL/min. Once a steady-state was achieved, which, depending on the flow rate, could take up to an hour from the moment the syringe pumps were activated, images were captured at multiple locations along the mixing channel using an exposure time of 100 ms.

2.3. Data collection and analysis

Once the system reached a steady-state, the mixing process's progress along the channel was quantified by collecting digital images at different cross-sections along the channel. Each image was analyzed using ImageJ software (Version 1.51k) to determine the pixel-by-pixel light intensity I_i across the selected cross-section width. Each image was a 16-bit grayscale image made of 2048 × 2048 pixels. Each pixel corresponded to an area of 0.5 μm × 0.5 μm. A calibration curve was separately constructed by measuring the light intensity of solutions of known FITC concentrations. The FITC concentration, C, was found to vary linearly with light intensity, I, in the FITC concentration range used here (0−1 mM), implying that $C = kI$, where k is the proportionality constant. This method was used to quantify the FITC tracer's distribution across selected cross-sections (Bend 2, Bend 4, and Bend 6 in Fig. 1E) along the channel. With this approach, we were able to quantify the cross-sectional FITC concentration profiles' evolution along the channel and hence quantify the mixing process's progress as the fluid advanced through the channel. To do so, the pixel light intensity I_i at point i was used to determine the normalized concentration ξ_i at that point using:

$$\xi_i = \frac{(C_i - C_{Min})}{(C_{Max} - C_{Min})} = \frac{(I_i - I_{Min})}{(I_{Max} - I_{Min})} \quad (1)$$

In this expression, the maximum FITC concentration, C_{Max}, corresponding to a pixel intensity I_{Max}, is the concentration value of the unmixed FITC solution, whereas the minimum concentration $C_{Min} = 0$ mg/L, corresponding to a pixel intensity I_{Min}, is the FITC concentration of the DI water solution. From this definition, it follows that $\xi_i = 1$ for any point occupied by

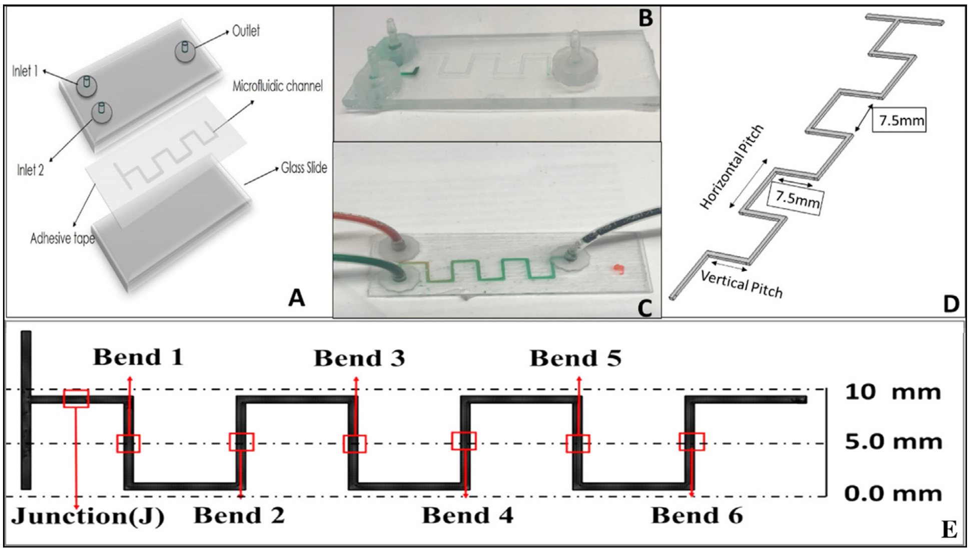

Fig. 1 – Schematic and actual images of the serpentine micromixing device used in this work: (A) Diagrammatic representation of the device showing top glass slide with inlet and outlet ports, middle microfluidic channel cut into of polyester tape, and bottom glass slide; (B) Assembled device prior to the insertion of inlet and outlet tubes; (C) Actual image of assembled device with red and green food coloring dyes flowing through the inlet tubes to visualize the flow pattern; (D) 3D CFD model of the channel in the device constructed in COMSOL; and (E) 2D geometric view of the channel showing the cross-sections where experimental concentration data were collected (Bend 2, Bend 4, and Bend 6) and where simulation results were collected (Junction (J), Bend 1, Bend 2, Bend 3, Bend 4, Bend 5 and Bend 6). (For interpretation of the references to colour in this figure legend, the reader is referred to the web version of this article.)

the unmixed FITC solution, $\xi_i = 0$ for any point occupied by the DI water, and, more in general, $0 \le \xi_i \le 1$ for any point in the system. Point-by-point values of I_i, and hence of C_i as well as ξ_i, along with selected cross-sections, were obtained and recorded for each experiment.

The degree of mixing achieved at any given cross-section was quantified using the mixing efficiency η, defined as (Cha et al., 2006; Jännig and Nguyen, 2011; Sivashankar et al., 2016):

$$\eta = 1 - \sqrt{\frac{1}{N}\sum_{i=1}^{N}(\sigma_i)^2} \quad (2)$$

where the dimensionless concentration deviation σ_l at the point l is defined as:

$$\sigma_i = \frac{(\xi_i - \xi_{Mix})}{(\xi_{Unmix} - \xi_{Mix})} \quad (3)$$

In this expression, ξ_i is as defined above, ξ_{Mix} is the ultimate value of the normalized concentration under complete mixing conditions (and equal to 0.5 here since the two streams being mixed have the same flow rate), and ξ_{Unmix} is the normalized concentration of the point i before mixing. In our case, the value of ξ_{Unmix} was either 0 or 1 depending, respectively, on whether the point was initially in the portion of the channel occupied by the distilled water ($\xi_{Unmix} = 0$) or in the FITC solution ($\xi_{Unmix} = 1$).

It is worth remarking that, at steady state, the mixing efficiency at any specific cross-section did not vary with time. Hence, by determining the mixing efficiency at progressively different cross-sections of the device, it was possible to follow the mixing process's progress along the channel. The mixing efficiency, especially the mixing efficiency value at the end of the device, was used to provide quantitative information on the device's degree of mixing.

3. Numerical simulations

3.1. *Numerical simulations of the mixing process in the microfluidic device*

Computational Fluid Dynamics (CFD) simulations were performed using COMSOL 5.3 to predict the microfluidic device's velocity flow field. This approach was also used to validate the computationally predicted concentration profiles by comparing them with the corresponding experimentally obtained profiles at different locations along the serpentine micromixer. Additionally, the CFD-predicted mixing efficiency was obtained and compared with that measured experimentally. CFD utilizes the fundamental momentum and mass conservation equations to describe the hydrodynamics of the process and predict the distribution of the tracer, i.e., the Navier-Stokes and continuity equations to obtain the fluid velocity distribution, and the convection-diffusion equation to obtain the concentration profile of the tracer under steady-state flow conditions (Chen et al., 2016).

The system geometry was constructed in COMSOL as depicted in Fig. 1D, and it was identical to the geometry of the experimental system. The cross-sectional area of the channel was rectangular (700 μm × 81 μm), and the serpentine channel shown in Fig. 1E was meshed using a fine-element grid. The computational domain representing the channel was divided into finite cells. Mesh-independence studies were conducted by running CFD simulations using grids containing different numbers of cells, from extra coarse (37,989 cells) to extra fine (999,447), to ensure that the computational results were not affected by the number of cells in the domain. As a result, the simulations used in the comparisons with the experimental results were conducted with a grid containing 405,527 cells, whereas those used in additional parametric studies to evaluate the system's sensitivity to critical design and operating parameters used a grid with 157,394 cells to reduce computational time. Details of the results of the mesh-independence study are presented in the Results section below.

The physics models applied to build the model in COMSOL were creeping flow and diffusional transport of diluted species. The boundary conditions at all solid surfaces were set to the no-slip condition (Patsis et al., 2012; Tretheway and Meinhart, 2002). The inlet streams were modeled to contain pure water and a 1 mM aqueous solution of FITC. Accordingly, the FITC concentrations at Inlet 1 and Inlet 2 were set as C = 0 mM and C = 1 mM, respectively. The two feed flow rates at the inlets were identical, and the resulting total flow rate through the channel, Q, was computationally set at either 0.1 μL/min or 10 μL/min, as in the experiments. The properties of both fluids used in the simulations were those of water at 20 °C, i.e., the fluids were Newtonian, and their density and viscosity were set to 1000 kg/m^3 and 1 mPa s, respectively. The diffusion coefficient for the FITC solute in water, D_{AB}, was assumed to be 0.64×10^{-9} m^2/s (Galambos and Forster, 1998). After meshing and setting up the system, COMSOL utilized a finite element method to conduct the simulations.

In addition to the CFD-simulations conducted for the same system and operating conditions used in the experiments (i.e., an 81-μm depth channel and two flow rates, i.e., Q = 0.10 μL/min and Q = 10 μL/min), additional simulations were conducted to determine the sensitivity of the mixing process (expressed as mixing efficiency) to an even higher flow rate (Q = 100 μL/min) and different channel geometries, i.e., for channel depths equal to 25 μm, 50 μm, 100 μm, 200 μm, and 400 μm, and different inlet geometries for which experiments were not conducted.

3.2. *Numerical simulations and analytical predictions of the mixing process in a straight channel*

Additional CFD simulations were carried out to quantify the role of the 90° elbows in the serpentine design on the mixing process. This was achieved by comparing the CFD-predicted mixing efficiency of the serpentine channel with that of a simple straight channel having the same length as the overall length of the serpentine channel (112 mm) and with the same width and depth. By comparing the numerically predicted mixing efficiency along the serpentine microdevice with that along the straight channel, it was possible to quantify each bend's contribution to the evolution of the mixing process in the serpentine channel.

A preliminary test of the correctness of COMSOL numerical predictions was conducted by comparing the numerically predicted mixing efficiency at the end of the above-mentioned straight channel with the predictions from a previously derived analytical expression (Lam et al., 2005), which had been obtained for the case of a fluid moving under a laminar regime in a rectangular channel containing a tracer subjected to molecular diffusion across the channel, but ignoring the mixing contributions of axial diffusion and Tyler-Aris dispersion. The analytical expression is (Lam et al., 2005):

$$C^* = \frac{1}{2} - \frac{2}{\pi}\sum_{n=1}^{\infty}\frac{(-1)^n}{(2n-1)}\cos\left[\frac{(2n-1)\pi x}{W}\right]e^{-[(2n-1)\pi]^2\frac{4z}{WPe}} \tag{4}$$

In this equation, Pe is the Peclet number ($\overline{u}W/D_{AB}$) calculated using the channel width (W), the flow rate per unit cross-sectional area ($\overline{u}$) and the FITC diffusion coefficient (D_{AB}), C^* is the non-dimensional tracer concentration ($C^* = (C'/C'_0)$), where C'_0 is the concentration of sample analyte inlet stream (1 mM), and C' is the sample concentration of the analyte at any given point in the microfluidic device. Eq. (4) shows that the non-dimensional tracer concentration at any point in the channel is a function of both x and z, where x is the coordinate in the direction of the channel width while z is the coordinate along the channel length. The origin was fixed at the channel inlet.

4. Results

4.1. *Experimental and computational results for the cross-sectional FITC concentration profiles along the channel*

Fig. 2 shows experimental images of the channel at the bend locations described in Fig. 1E, labeled here as Bend 2, Bend 4, and Bend 6, at flow rates of 0.1 μL/min and 10 μL/min, respectively. In this figure, the FITC dye can be observed as a bright region, while the distilled water occupies the dark region. The channel background is shown with green dotted lines delineating the device from the background. The red line indicates the direction of flow. It is worth noticing that the bright regions were restricted to the channels at both flow rates, indicating no seeping of the solution through the adhesive tape. As can be observed visually in Fig. 2, the fluorescent zone's size across any selected cross-section perpendicular to the flow progressively increased as one moved further away from the channel inlet. This was the result of the diffusion and mixing processes of the dye across the channel width.

A quantitative determination of the progression of the cross-sectional mixing process along the channel was conducted as described above to obtain the tracer concentration as a function of the position x along the cross-sections at each of the three different cross-sections along the channel at each of the three selected bend locations shown where experimental measurements were made (Fig. 1E). The experimental FITC concentration profiles as a function of width coordinate x for different bend locations and flow rates equal to 0.1 μL/min and 10 μL/min, respectively, are reported in Fig. 3. Although not shown in this figure, at the inlet of the serpentine channel, the FITC occupied one half of the channel (0 μm < x < 350 μm), where the FITC concentration was 1 mM, while the other half (350 μm < x < 700 μm) contained no dye, i.e., the initial FITC concentration in the channel was a step function of x, jumping down from 1 mM to 0 mM at x = 350 μm. Fig. 3 shows that the experimental concentration profiles become progressively flatter as one moves along the channel since the dye migrates in the cross-sectional direction from the high-concentration region to the low concentration region. This is the result of the mass transfer process caused by molecular diffusion and the additional mixing effects introduced by the flow alteration resulting from the sharp 90° elbows in the serpentine. By comparing the experimental FITC concentration profiles at the two different flow rates in Fig. 3, one can also see that the concentration profiles obtained at the lower flow rate (0.1 μL/min) are flatter than those at, the higher flow rate (10 μL/min) at the same bend location, which can be expected since the residence time of the fluid in the micromixer is much longer in the former case and, as a result, the diffusion process can occur over a longer period of time.

The FITC concentration profiles were also computationally predicted using COMSOL at the same bend locations

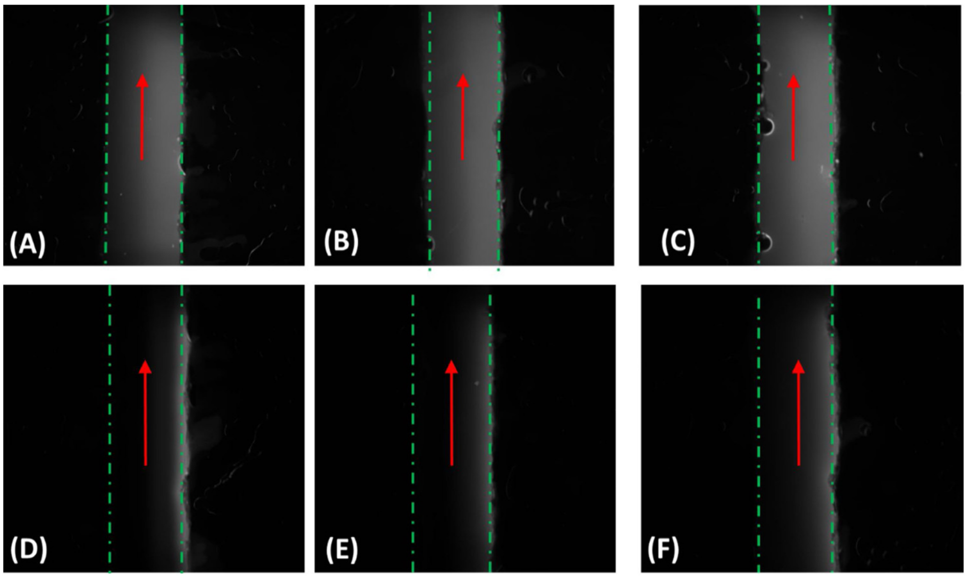

Fig. 2 – Fluorescence images showing the progressive migration of the FITC dye in the channel at the three positions long the serpentine (Bend 2, Bend 4 and Bend 6, as marked in Fig. 1E), at different flow rates. For each channel, the dotted green lines delimit the effective area of the channel marking the channel boundaries. The direction of flow is indicated by the red line in the image: (A) Bend 2, 0.1 μL/min; (B) Bend 4, 0.1 μL/min; (C) Bend 6, 0.1 μL/min; (D) Bend 2, 10 μL/min; (E) Bend 4, 10 μL/min; (F) Bend 6, 10 μL/min. (For interpretation of the references to colour in this figure legend, the reader is referred to the web version of this article.)

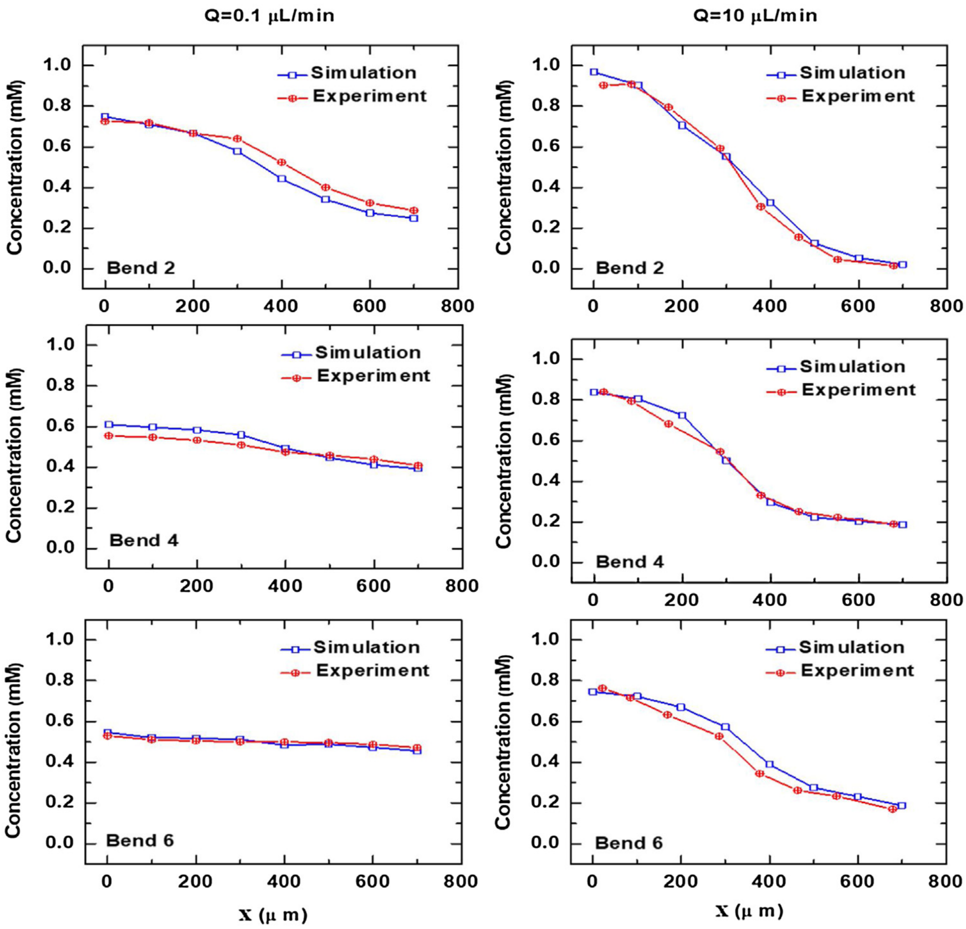

Fig. 3 – Experimental concentration profiles obtained from fluorescent images at Bend 2, Bend 4, and Bend 6 for flow rates equal to 0.1 μL/min and 10 μL/min, respectively, and corresponding concentration profiles obtained from COMSOL simulations.

as in the experiments and are reported in Fig. 3. In general, the agreement between computational and experimental results is good. However, one can see that the experimental concentrations are slightly lower than the corresponding numerical predictions, which is consistent with the impossibility of eliminating all geometric variability in any real experiments that would result in a slightly improved mixing performance. These results also imply that mixing appears slightly better in the experimental system than in the simulations. However, overall, there is a significant agreement between the experimental results and the numerical predictions at all locations and at both flow rates, which supports the experimental method's validity and the correctness of the numerical approach used here. This agreement also validates the computational approach and provides evidence that the computational method can be effectively used to simulate the process, possibly even in operational regions and design ranges not covered in the experimentation.

The evolution of the concentration profiles obtained with the COMSOL simulations is presented in Fig. 4, in which the FITC concentration at Inlet 1 (0 mM; DI water) is represented with a dark blue color, and the concentration at Inlet 2 (1 mM) is represented in dark red. One can see that the concentration profile in the lower flow rate system turned green (indicating that the FITC concentration approached the 0.5 mM value) much more closely to the device inlet compared to the higher flow rate case. The middle band was green while it was still red and blue near the walls, indicating a significant concentration gradient across the channel even at the system's outlet.

4.2. *Experimental and computational results for the mixing efficiency of the serpentine micromixer*

The experimental and computational concentration profiles were additionally used to calculate the mixing efficiency, η, for the serpentine device using Eq. (2). To ensure that the computational results did not vary with the mesh size used in the simulations, a mesh-independence study was first conducted. The mixing efficiency at the various bends were numerically obtained for six different mesh configurations, i.e., extra coarse (37,989 cells), coarser (50,993 cells), coarse (75,624 cells), normal (114,929 cells), fine (157,394 cells), finer (405,527 cells), and extra fine (999,447). The results, shown in Fig. 5A, indicate that the predicted mixing efficiency was highly dependent on mesh size. However, this figure also shows that the profiles obtained with the fine, finer, and extra fine mesh sizes were similar (i.e., within ±7% of each other), i.e., that mesh independence was reached, especially when the finer and extra fine mesh sizes were used. Therefore, the finer mesh (405,527 cells) was used to obtain numerical results for the same systems used in the experiments to ensure that accurate numerical prediction would be compared with the experimental results. However, the parametric studies in which the only relative importance of geometric and operating parameters was assessed were conducted using the fine mesh (157,394 cells) to obtain a significant number of computational predictions in a reasonable time without compromising the validity of the results.

The mixing efficiency at the two different flow rates is presented in Fig. 5B as a function of the channel's distance (reported as bend number). One can see that the agreement between predicted and experimental η values in the serpentine channel is substantial at both flow rates and across the entire channel length. Table 1 provides additional details about the Reynolds numbers and Peclet numbers and the final mixing efficiencies at Bend 6 in the same system. Significant mixing was achieved in the serpentine channel immediately after the first three 90° elbows, i.e., at Bend 1 (computational results only) and after the first seven elbows, i.e., at Bend 2 (computational and experimental results). The other 90° elbows' presence further increased the device's mixing efficiency (Bend 3 and higher) by Slowing down the flow rate, and thus increasing the residence time and the time available for mixing and diffusion to take place, significantly improved mixing efficiency, as one can see by comparing the two panels in Fig. 5B and Table 1. For the 10 μL/min case, a 67.4% mixing efficiency was achieved by the end of the serpentine channel, while at 0.1 μL/min, a 96.0% mixing efficiency was achieved.

To further quantify the effects of the 90° elbows, the mixing efficiencies for the serpentine design were compared against the mixing efficiencies obtained in a straight channel with no elbows but with the same overall length, cross-section, and depth as the serpentine. This was first accomplished computationally using the COMSOL simulations for the straight channel. The results are also shown in Fig. 5B and Table 1. For flow rates equal to 0.1 μL/min and 10 μL/min, the mixing efficiency at the end of the straight channel was 63.6% and 21.5%, respectively, which is significantly lower than the values obtained from the serpentine channel (95.9% and 66.1%, respectively). This demonstrates that the 90° elbows in the serpentine design are the critical feature responsible for increasing the straight channel's mixing efficiency. To further validate the COMSOL predictions for the straight channel, the mixing efficiency in this channel was determined using the analytical predictions for the concentration based on Eq. (4). This equation was numerically solved using MATLAB for different points along the channel's width (x) and at the different cross-sections along the straight channel (z). The corresponding results for η are also shown in Fig. 5B and Table 1. One can see that, in general, the COMSOL computational results and the analytical predictions are in significant agreement even for this case.

Fig. 5B can also be used to provide a qualitative understanding of the impact of the initial T-junction to initially contact the fluids at the device inlet on the mixing process. The straight channel results show an appreciable initial increase in the mixing efficiency compared to the remaining portion of the channel. Although the mixing efficiency cannot be expected to be a linear function of the distance traveled by the fluid, this initial jump could be attributed to the T-junction. However, by comparing this increase with the much more significant increase in the mixing efficiency at Bend 1 in the serpentine system, one can conclude that the first elbow plays a critical role in producing a rapid increase in the mixing efficiency, possibly even amplifying the initial contribution of the T-junction to mixing.

Since the integrity of the micromixing device could be potentially compromised by an excessive pressure building up during an operation in the device assembly, the pressure drop along the serpentine channel, i.e., the difference between the inlet pressure and the pressure at any specific length along the channel at the desired flow rate, was computationally predicted. Of particular relevance here is the maximum pressure drop between the inlet and the outlet since the inlet's resulting maximum absolute pressure could affect the device's integrity. Fig. 5C shows the calculated pressure drop at the two different flow rates studied as a function for the different bend numbers, i.e., along the channel length. At the lower flow rate, the maximum pressure drop was minimal (~30 Pa), and even for Q = 10 μL/min, the corresponding figure was on the order of 3 kPa. Such modest increases in the pressure inside the channel can be expected to have no impact on the device's mechanical integrity. This conclusion was experimentally validated in separate experiments in our laboratory, not related to the

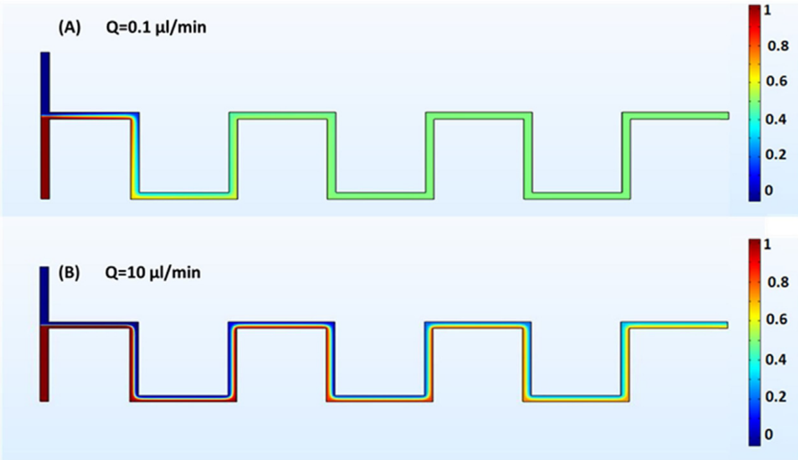

Fig. 4 – COMSOL simulations showing the FITC concentration profiles in a channel having the same geometry as the experimental system for two different flow rates, (A) Q = 0.1 µL/min and (B) Q = 10 µL/min. Color scale varies between 1 mM (dark red) and 0 mM (dark blue). (For interpretation of the references to colour in this figure legend, the reader is referred to the web version of this article.)

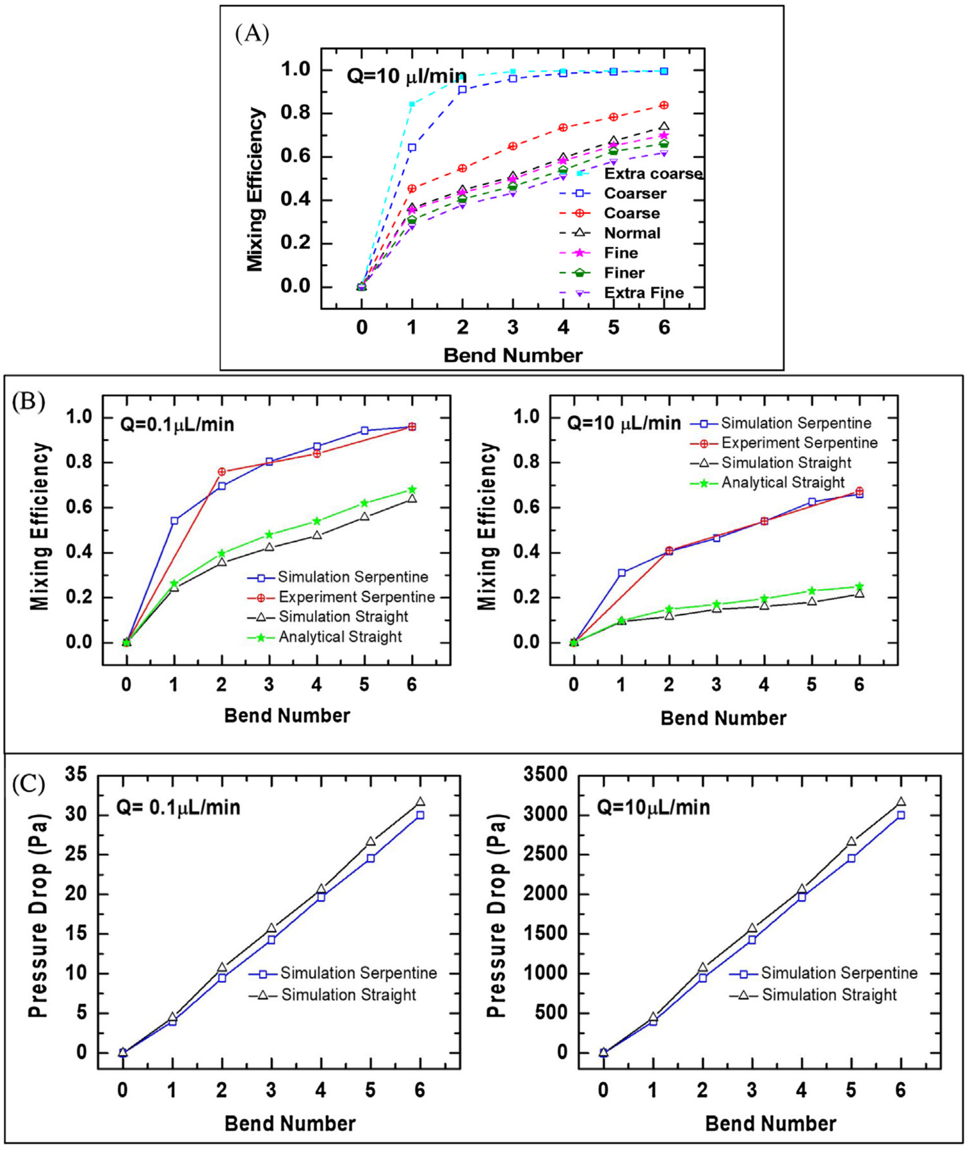

Fig. 5 – (A) Mixing efficiency at different bends in the serpentine micromixing device at a flow rate of 10 µL/min using different mesh configurations; (B) Mixing efficiency at different bends in the serpentine micromixing device and in a straight channel of identical length and depth at flow rates of 0.1 µL/min and 10 µL/min, respectively; (C) Pressure drop at different bends in the serpentine micromixing device and in a straight channel of identical length and depth at flow rates of 0.1 µL/min and 10 µL/min, respectively.

Table 1 – Comparison between the CFD-predicted simulation values and the experimental results for the mixing efficiency, η at Bend 6 for the serpentine device (81 μm depth) and between the CFD-predicted simulation values and the analytical solutions for the mixing efficiency, η for the straight channel (same length and depth as serpentine device).

Flow rate	Reynolds number	Peclet number	η (experimental; serpentine)	η (simulation; serpentine)	η (simulation; straight channel)	η (analytical; straight channel)
0.1 μL/min	0.015	23.4	96.0%	95.9%	63.6%	68.2%
10 μL/min	1.5	2340	67.4%	66.1%	21.5%	25.7%

present work, in which a microdevice somewhat similar to the serpentine device used here was subjected to increasing pressure drops up to 116 kPa (1.14 atm) without compromising the integrity of the device (results not shown). These results are in line with the experimental results of other investigators who have reported that the tensive force per area required to delaminate the adhesive tape used here (Arcare® 90,445) when bonded to glass was about 700 kPa and that the microdevices that they tested were stable for weeks even under physiological shear force conditions (Kratz et al., 2019). In summary, it can be concluded that the integrity of the micromixing device would not be compromised by excessive pressure drop during operation.

Fig. 5C also presents the corresponding pressure drops along the straight channel. A comparison of the two systems' profiles shows that the serpentine channel's pressure drop was only marginally higher than in the straight channel, implying that the 90° elbows in the serpentine design contributed only modestly to increasing the pressure drop.

The results in Fig. 5 can be used to calculate the mixing cost, *mc*, defined as the ratio of the pressure drop to achieve a given mixing efficiency to the mixing efficiency expressed in percentage (%) (Ortega-Casanova and Lai, 2018):

$$mc = \frac{\Delta P}{\eta\,(in\,\%)} \tag{5}$$

implying that the units for *mc* are Pa/%. For the 0.1 μL/min case (Re = 0.015; Sc = 1562) *mc* varied between 0.13 Pa/% at Bend 2 (η = 75%) to 0.31 Pa/% at Bend 6 (η = 96%), whereas for the 10 μL/min case (Re = 1.5; Sc = 1562) *mc* varied between 23.3 Pa/% at Bend 2 (η = 40%) to 45.4 Pa/% at Bend 6 (η = 67.4%). These values are typically larger than those achieved with very intricate micromixing designs but are on the same order of magnitude as those obtained with less complex structures. For example, Ortega-Casanova and Lai (2018) obtained very low *mc* values, ranging from 0.05 Pa/% (Re = 0.1; η = 95%) to 0.15 Pa/% (Re = 0.29; η = 85%), using their complex multiple-input micromixer. However, other investigators obtained higher *mc* values (~1–20 Pa/%) using other types of micromixers (Chung and Shih, 2007; Hsiao et al., 2014; Khosravi Parsa et al., 2014; Ortega-Casanova, 2016, 2017a, 2017b; Sadegh Cheri et al., 2013; Salas and Ortega-Casanova, 2016). A detailed comparison of *mc* values for different configurations is presented elsewhere (Ortega-Casanova and Lai, 2018).

5. Discussion

Although previous work on serpentine channels has been reported (Ammar et al., 2014; Sivashankar et al., 2016), the determination of each elbow's contribution to the mixing process has not been presented in the literature. Furthermore, previous studies have focused on flow rates that are on the order of about 1 mL/min (Sivashankar et al., 2016) and not on low flow rates (on the order of μL/min) that are typical for most microfluidic devices whose volumes are in μL (including ours, which has a volume of 6.35 μL). Therefore, in this work, we studied a low-volume microfluidic device, and we examined the contribution of each elbow of the serpentine channel to the mixing efficiency.

Since the experimental measurements validated the COMSOL predictions, further analysis of the impact of other design and operating parameters could be reliably conducted using only a similar computational approach. Although the effect of varying several parameters on mixing efficiency could in principle be studied, here we examined primarily the impact of channel depth since there have been very few studies exploring the effect of this variable on mixing effectiveness (Buchegger et al., 2011; Chen et al., 2016). In addition, concentration profiles are difficult to obtain experimentally using microscope tracer analysis as the channel depth is increased, thus making computational predictions even more valuable. Therefore, in this work, COMSOL simulations were carried out for five additional channel depths (in addition to the 81 μm-deep channel), i.e., 25 μm, 50 μm, 100 μm, 200 μm, and 400 μm and at flow rates equal to 0.1 μL/min, 10 μL/min, and, additionally, 100 μL/min (also for the 81 μm-deep channel). The resulting mixing efficiencies of the serpentine micromixer for these different channel depths and flow rates are shown in Fig. 6. These results indicate that increasing the channel depth results in a negligible impact on mixing efficiency if the channel depth is in the range 25–81 μm, or slightly above (100 μm). However, the CFD simulations predict a significant increase in mixing efficiency when the channel depth is increased to 200 μm and 400 μm. This increase is explained in some detail below. It is worth noticing that for a channel depth of 50 μm, the Reynolds number is equal to 0.01, 1, and 10, when Q = 0.1 μL/min, Q = 10 μL/min, and Q = 100 μL/min, respectively, while for channels with depths equal to 25 μm, 50 μm, 81 μm,100 μm, 200 μm and 400 μm at 10 μL/min the Reynolds numbers are 0.5, 1, 1.5, 2, 3.6, and 5.9 respectively. The Schmidt number ($\mu/(\rho D_{AB})$) for the fluid is 1562.

To further understand the effect of the channel's depth, detailed COMSOL simulations were carried out to determine the flows in channels of different depths. Fig. 7 shows the COMSOL-predicted streamlines in the channel for different depths of the channel, namely, (A) 400 μm, (B) 200 μm, (C) 150 μm, and (D) 100 μm. Vector diagrams on cross-sectional areas immediately following the T-junction and after the first four elbows are shown in the inserts. The vector diagrams provide a visual display of the quality of mixing at cross-sections of interest in the microfluidic device. The slice plots show the mixing efficiency before the 90° elbow. The degree of mixing achieved at this and other cross-sections along the channel was quantified using the mixing efficiency η as defined above. Fig. 7 shows the mixing efficiency for various designs with various depths at flow rate Q = 10 μL/min. Furthermore, the vector diagram made us specifically interested in the initial elbows.

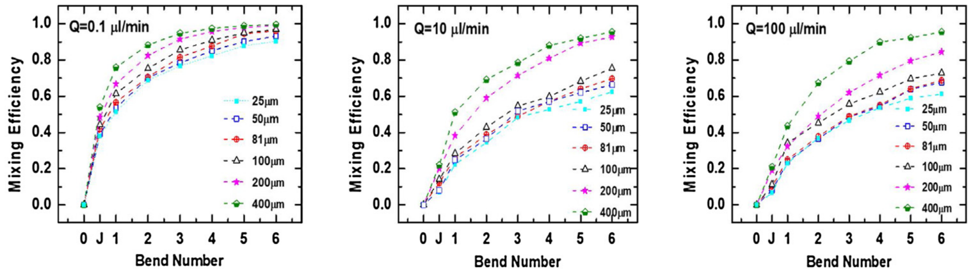

Fig. 6 – Mixing efficiency obtained using COMSOL simulations for different depths of the channel (25, 50, 81, 100, 200 and 400 μm) at flow rates of 0.1 μL/min, 10 μL/min, and 100 μL/min.

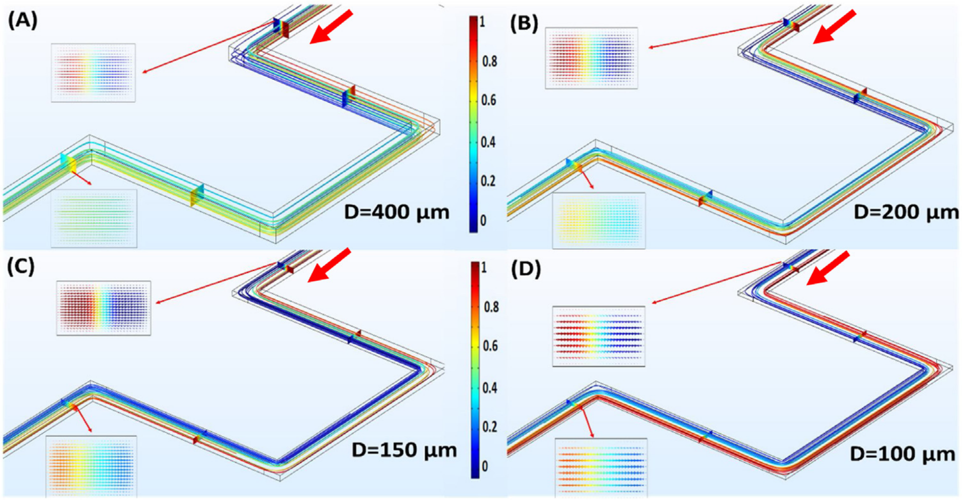

Fig. 7 – COMSOL simulations showing the streamlines in the channel cross-sectional areas immediately following the T-junction and after the first four elbows for different channel depths. Vector diagrams at selected cross-sections are shown in the insert: (A) 400 μm, (B) 200 μm, (C) 150 μm, and (D) 100 μm. Red arrow indicate the direction of the flow in the channel. (For interpretation of the references to colour in this figure legend, the reader is referred to the web version of this article.)

It is important to notice that channel shape effects dominate at higher Reynolds number (as seen in Figs. 6 and 7 for Q = 10 μL/min). At 10 μL/min and channel depths larger than 200 μm, a relative well-mixed behavior can be observed immediately after the first elbow. This can be explained by calculating the Dean number, De, defined as $De = Re\sqrt{D_h/2r_c}$, where Re is Reynolds number, D_h is the hydraulic diameter (= $2W{\cdot}D/(W{\cdot}D)$), and, r_c is the radius of curvature. The Dean number is a measure of the secondary flows occurring in the channel. At high Reynolds number or large hydraulic diameters, secondary flows dominate. The secondary flows are generated in the elbows due to centrifugal forces that drive the fluid motion towards the outer walls, thus creating velocity and pressure gradients that cause vorticial flows (Chen et al., 2016; Lee et al., 2016). Hence, for microchannels of depth greater than 200 μm and at a higher flow rate (10 μL/min), the Dean number becomes important, and the effect of secondary flows on mixing efficiency becomes dominant. These effects become more significant as the channel depth increases, as shown in Fig. 7. However, for smaller channel depths, the mixing efficiency is much poorer (Fig. 6). Indeed, for channels with shallow depth, the mixing efficiency is almost independent of the channel depth, as mentioned above.

It is important to notice that the mixing efficiency at very low Reynolds numbers (Re = 0.01 for Q = 0.1 μL/min) improves significantly after the first 90° elbow for all channel depths, unlike that at Q = 10 μL/min, as it can be seen in Figs. 6 and 7. This seems to indicate that transverse diffusion effects dominate at low flow rates (or high residence times) (Lee et al., 2016). Under such conditions, just a few elbows in the serpentine channel will be enough to achieve relatively high mixing efficiency levels. Furthermore, as transverse diffusion becomes dominant over the Dean effects, the mixing efficiency does not show any shape-dependent behavior. As shown in Fig. 6, even channels with shallow depths achieve significant mixing efficiency. This observation leads to the conclusion that for small depths of the microfluidic channels (~25 to 81 μm), improved mixing can be achieved using lower flow rates to ensure a long enough residence time for transverse diffusion to dominate since chaotic advection from secondary flows is typically negligible for channels of such small depths. For larger flow rates, the depth of the channel must be increased to achieve higher mixing efficiency. Hence, at a flow rate of 10 μL/min, it is also important to determine whether other design factors affect the mixing efficiency. The 10 μL/min flow rated was used in the computations since, at 0.1 μL /min, the mixing efficiency increases drastically and can mask any variation in mixing efficiency caused by the different designs.

Therefore, to further understand the mixing efficiency contribution resulting to the different designs, additional COMSOL simulations were conducted by varying the length of the channels between two consecutive 90° elbows, which we define here as "pitch," following the nomenclature used by mechanical engineers to describe the distance between repeated elements in a structure. Therefore, here we labeled as "vertical pitch" the length of the all serpentine arms aligned in the same direction as the overall flow in the micromixer (i.e., along the long dimension of the micromixer assembly) and as

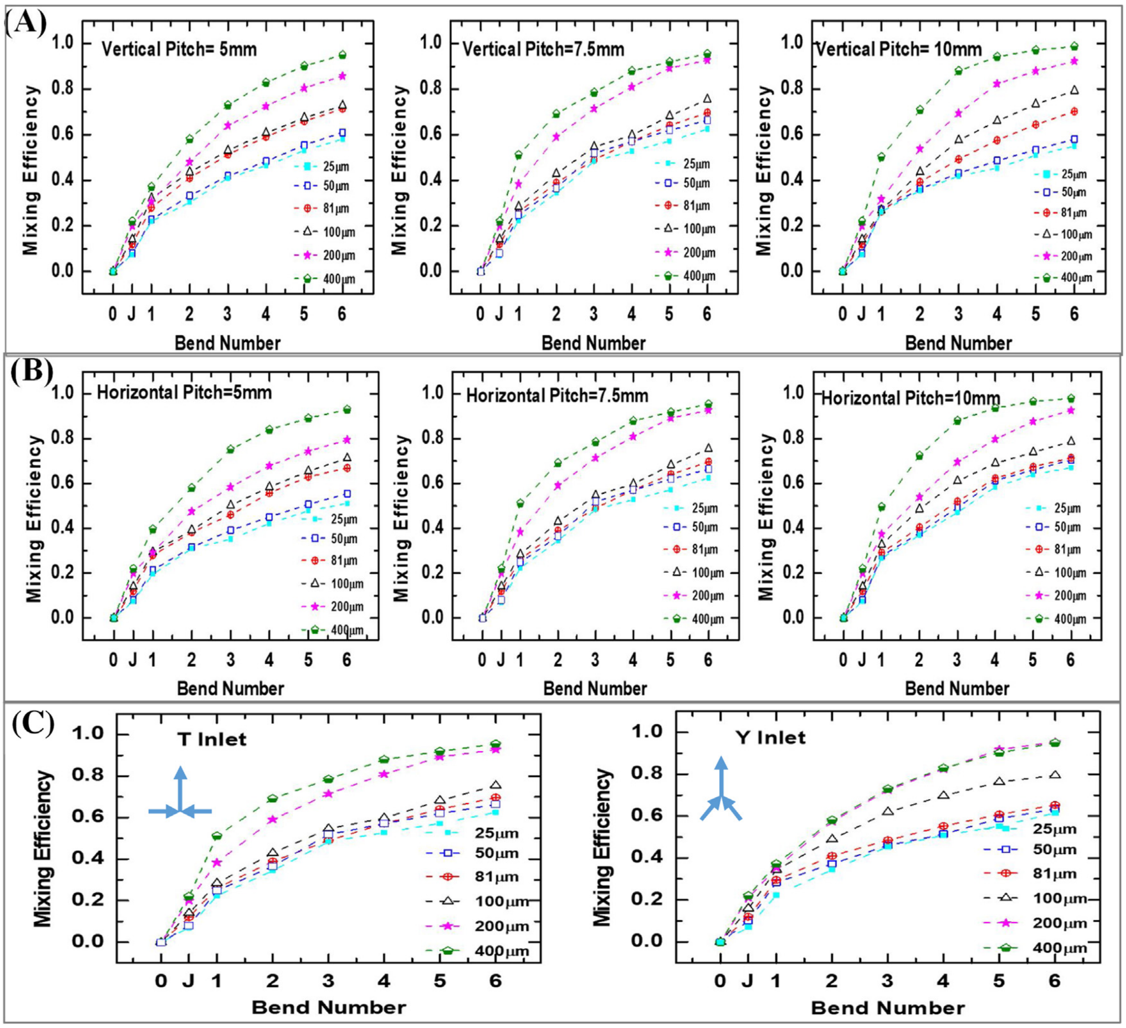

Fig. 8 – Mixing efficiency obtained using COMSOL simulations for different depths of the channel (25, 50, 81, 100, 200 and 400 μm) at a flow rate of 10 μL/min; (A) For three different vertical pitches (5 mm, 7.5 mm and 10 mm); (B) For three different horizontal pitches (5 mm, 7.5 mm and 10 mm); (C) For two different inlet shapes (T-junction and Y-junction).

"horizontal pitch" the length of the all serpentine arms in a direction perpendicular to the overall flow in the micromixer (i.e., along the short dimension of the micromixer assembly), as visually shown in Fig. 1D. In our standard design, both pitches were 7.5 μm. In addition, we also explored the effect of the initial inlet design, where the two feed streams meet by determining the effect of using a Y-junction instead of the T-junction used in the experiments. The results presented in Fig. 8A and B indicate that changing the vertical pitch or the horizontal pitch in the range 5−10 μm has a minimal impact on the mixing efficiency. The slight variations observed in those figures can be attributed to a change in the overall length of the serpentine channel introduced by the larger pitches. Consequently, the drastic increase in mixing efficiency associated with different designs can be attributed primarily to the elbows' presence. The impact of the change in the inlet design (standard T-junction vs. Y-junction) is shown in Fig. 8C, where the channel depth is used as a parameter. The T-inlet appears to improve mixing in the initial bends better than the Y-inlet. This effect is more evident in channels or greater depth (200 μm and above).

Fig. 9 provides a more direct comparison of the mixing efficiency for various design architectures, including different channel depths and inlet types. As already mentioned, the higher mixing efficiency associated with the increase in the vertical pitch or the horizontal pitch to 10 mm can likely be attributed to the increase in the serpentine channel's overall length.

This point is further supported by the results presented in Fig. 10A, which shows the mixing efficiency for different design architectures as a function of the fluidic path length, i.e., the distance traveled by the fluid in the whole microdevice. In general, it appears that different designs have similar, although not identical, mixing efficiencies for identical path lengths. The design with 5 mm horizontal and vertical pitches has a slightly better mixing efficiency in terms of relative length at Q = 10 μL/min and a channel depth of 81 μm. Generally, shorter pitch designs appear to be superior to those with longer pitches, as far as mixing is concerned, for similar path lengths. This is consistent with the other findings in this work, indicating that the 90° elbows are primarily responsible for the improved mixing efficiency. This observation, in turn, suggests that a more efficient way to reduce the size of the micromixing device while maximizing mixing efficiency is to pack as many 90° elbows as possible on the chip. The limiting factor for such a case would be the resolution of the Cricut cutting machine. Since the shortest cuts achievable with this device are on the order of 1 mm, there is a significant room for future design

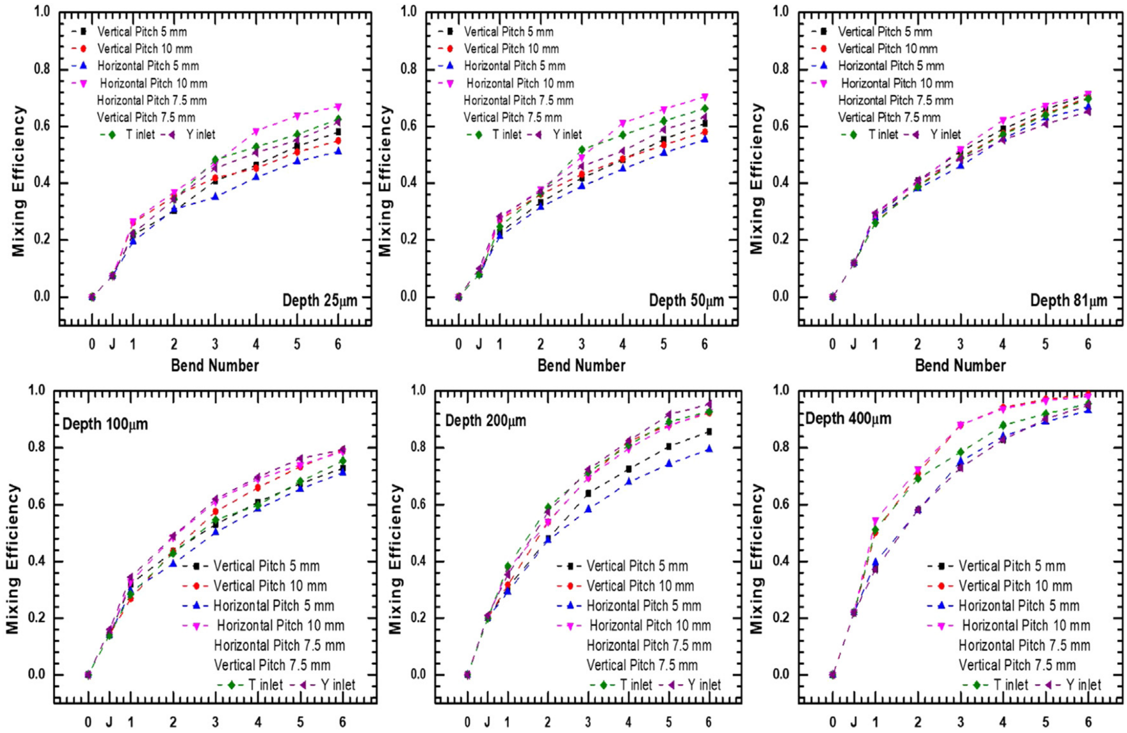

Fig. 9 – Mixing efficiency obtained using COMSOL simulations for different vertical pitches, horizontal pitches, and inlet design for different depths of the channel (25, 50, 81, 100, 200 and 400 μm) at a flow rate of 10 μL/min.

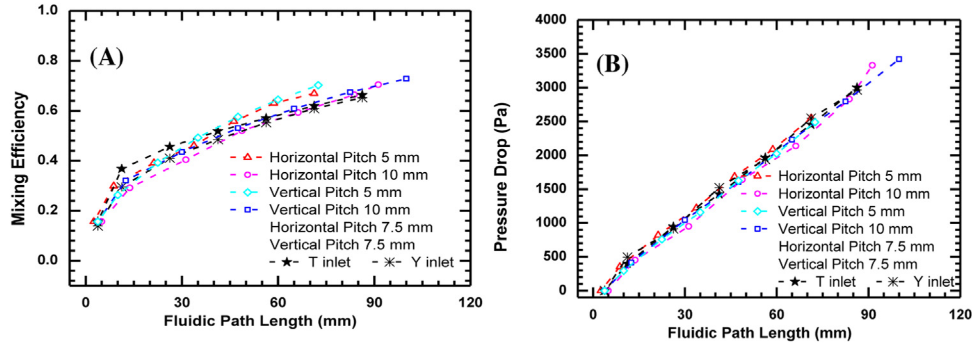

Fig. 10 – Results obtained using COMSOL simulations for different vertical pitches, horizontal pitches, and inlet designs for the 81 μm-deep channel at a flow rate of 10 μL/min: (A) Mixing efficiency as a function of the fluidic path length. (B) Pressure drop as a function of the fluidic path length.

improvements to maximize the number of 90° elbows while avoiding possible liquid seepage during the device assembling process.

In Fig. 10B, the pressure drop across the device for various architectures is shown as a function of fluidic path length. In all cases, the overall pressure drop is only modest and much lower than the tensive force per area required to delaminate the adhesive tape from the supporting glass, reported to be about 700 kPa (Kratz et al., 2019), implying that the mechanical integrity of these devices would not be compromised. These results and the results shown in Fig. 5C for the predicted pressure drop in the apparatus experimentally tested in this work indicate that additional bends in the serpentine design while maintaining the same path length, contribute only moderately to the overall pressure drop across the serpentine but improve the mixing efficiency of the device (Fig. 5B) significantly. This observation further confirms that future improvements in the basic design could simply require increasing the number of bends in the serpentine to increase its mixing efficiency while only modestly increasing the pressure drop, thus reducing the mixing cost *mc* of the device.

Finally, Fig. 11 presents the contribution of each bend in the serpentine to the overall mixing efficiency. In this figure, the mixing efficiency achieved in each bend was normalized to the overall mixing efficiency of that channel architecture, i.e., it was calculated as the mixing efficiency achieved just by that bend dived by overall mixing efficiency for the entire channel. The channel architecture considered in Fig. 11 is a T-inlet with a horizontal and vertical pitch of 7.5 mm. This figure clearly shows that the mixing efficiency of Bend 1 was always higher than that of any other bend for any given system. Furthermore, at lower flow rates, significant mixing occurred just in the first two bends. The number of bends needed for mixing increased progressively with increasing flow rates and decreases with increasing channel depth. Therefore, Fig. 11 can be used as a useful guide by researchers to design a serpentine microfluidic channel with a required mixing efficiency.

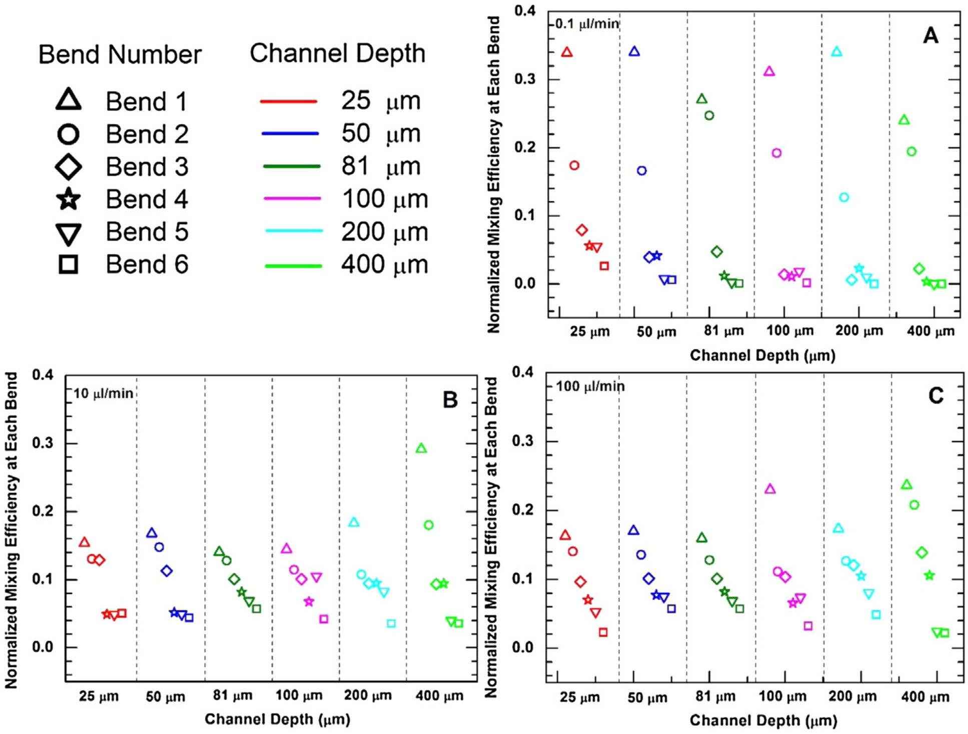

Fig. 11 – CFD-predicted normalized mixing efficiency of each individual bend for a channel with a T-inlet and a horizontal and vertical pitch of 7.5 mm, for different channel depths (25, 50, 81, 100, 200 and 400 μm) and flow rates equal to 0.1 μL/min (Panel A), 10 μL/min (Panel B) and 100 μL/min (Panel C). The mixing efficiency shown here was normalized, as described in the text.

6. Conclusion

In this work, we have shown that a highly effective serpentine micromixing device can be easily and inexpensively built using a technique based on thin, pressure-sensitive, double-sided adhesive flexible films and a cutter plotter. The approach proposed here would make microfluidic mixers straightforward in their fabrication, economical, and readily available in most laboratories without the need for highly skilled personnel, extensive training, and dedicated and costly fabrication equipment.

The microdevice built here was experimentally tested by observing the evolution of the mixing process of two miscible fluids, one containing a fluorescent dye tracer, through the collection of digital microscopic images at different cross-sections along the micromixing channel. The mixing efficiency of the device was obtained from the experimental concentrations of the fluid across different sections along the channel. These experimental data compared very favorably with the numerical solutions for the concentration profiles obtained using CFD simulations using COMSOL. Specifically, the CFD-computed velocity field was used in conjugation with the convection-diffusion equation to determine the mixing process's evolution occurring in these channels. The predictions from the COMSOL simulations were validated experimentally using the concentration of fluorescent dye tracer. Mixing efficiency was determined from both the experiments and the numerical computations.

This numerical approach was then used to test similar design architectures with different geometric characteristics. The micromixing channel's depth was computationally shown to play a minor role in the mixing process for low channel depths (25–81 μm). However, larger channel depths (100–400 μm) were associated with establishing secondary flows (Dean vortices), leading to improved mixing efficiency. It was determined that at higher flow rates and deeper microchannels, secondary flows dominate. These secondary flows lead to improved advection, which can significantly increase the mixing efficiency. However, at low flow rates, transverse diffusion dominates. It was determined that for small-sized microchannels on the order of 25–81 μm, mixing efficiency is dominated by transverse diffusion and not secondary flows. Hence, to achieve a high degree of mixing in small microchannels, it is advantageous to operate the device at high residence times to allow transverse diffusion to achieve the desired cross-sectional mixing level. Also, a T-junction to initially contact the fluids at the microdevice inlet was found to be superior, as far as mixing efficiency is concerned, to a Y-junction.

Both the experiments and the numerical simulations showed that the mixing efficacy was primarily associated with the number of 90° elbows in the device rather than the length of the straight sections of the serpentine. In particular, the first bend in the serpentine was the most critical of all the bends in the design. This observation suggests that future design improvements should focus on incorporating as many 90° elbows as possible on the chip to maximize mixing efficiency and further reduce the size of the micromixing device.

Declaration of interest statement

The authors declare no competing financial interests.

Acknowledgments

This manuscript is supported by Sagnik Basuray's NSF grant # 1751795, Career: "ASSURED" electrochemical platform for multiplexed detection of Cancer Biomarker Panel using Shear Enhanced Nanoporous Capacitive Electrodes and a New Jersey

Health Foundation Grant, # PC 54-20, "ESSENCE — A Selective and Sensitive Electrochemical POC Platform for Liquid Biopsy".

References

Afzal, A., Kim, K.-Y., 2012. Passive split and recombination micromixer with convergent–divergent walls. Chem. Eng. J. 203, 182–192.

Afzal, A., Kim, K.-Y., 2015. Convergent–divergent micromixer coupled with pulsatile flow. Sens. Actuators B: Chem. 211, 198–205.

Ahmed, D., Mao, X., Juluri, B.K., Huang, T.J., 2009. A fast microfluidic mixer based on acoustically driven sidewall-trapped microbubbles. Microfluid Nanofluid 7, 727.

Ammar, H., Ould el Moctar, A., Garnier, B., Peerhossaini, H., 2014. Flow pulsation and geometry effects on mixing of two miscible fluids in microchannels. J. Fluids Eng. 136, 121101-121101-121109.

Ansari, M.A., Kim, K.-Y., 2010. Mixing performance of unbalanced split and recombine micomixers with circular and rhombic sub-channels. Chem. Eng. J. 162, 760–767.

Ansari, M.A., Kim, K.-Y., Anwar, K., Kim, S.M., 2010. A novel passive micromixer based on unbalanced splits and collisions of fluid streams. J. Micromech. Microeng. 20, 055007.

Bartholomeusz, D.A., Boutte, R.W., Andrade, J.D., 2005. Xurography: rapid prototyping of microstructures using a cutting plotter. J. Microelectromech. Syst. 14, 1364–1374.

Buchegger, W., Wagner, C., Lendl, B., Kraft, M., Vellekoop, M.J., 2011. A highly uniform lamination micromixer with wedge shaped inlet channels for time resolved infrared spectroscopy. Microfluid. Nanofluid. 10, 889–897.

Campisi, M., Accoto, D., Damiani, F., Dario, P., 2009. A soft-lithographed chaotic electrokinetic micromixer for efficient chemical reactions in lab-on-chips. J. Micro Nano Mechatron. 5, 69–76.

Capretto, L., Cheng, W., Hill, M., Zhang, X., 2011. Micromixing within microfluidic devices. In: Microfluidics. Springer, pp. 27–68.

Cha, J., Kim, J., Ryu, S.-K., Park, J., Jeong, Y., Park, S., Park, S., Kim, H.C., Chun, K., 2006. A highly efficient 3D micromixer using soft PDMS bonding. J. Micromech. Microeng. 16, 1778.

Chen, X., Li, T., Zeng, H., Hu, Z., Fu, B., 2016. Numerical and experimental investigation on micromixers with serpentine microchannels. Int. J. Heat Mass Transf. 98, 131–140.

Cheng, Yu-Hsuan, et al., 2019. Effect of electrode configuration on the sensitivity of nucleic acid detection in a non-planar, flow-through, porous interdigitated electrode. Biomicrofluidics 13, 064118, http://dx.doi.org/10.1063/1.5126452, In press.

Cheng, Yu-Hsuan, et al., 2020. Metal–organic framework-based microfluidic impedance sensor platform for ultrasensitive detection of perfluorooctanesulfonate. ACS Appl. Mater. Interfaces 12 (9), 10503–10514, http://dx.doi.org/10.1021/acsami.9b22445.

Chung, C.K., Shih, T.R., 2007. A rhombic micromixer with asymmetrical flow for enhancing mixing. J. Micromech. Microeng. 17, 2495–2504.

Chung, C.-K., Shih, T., Wu, B., Chang, C., 2010. Design and mixing efficiency of rhombic micromixer with flat angles. Microsyst. Technol. 16, 1595–1600.

Du, Y., Zhang, Z., Yim, C., Lin, M., Cao, X., 2010. Evaluation of floor-grooved micromixers using concentration-channel length profiles. Micromachines 1, 19–33.

Fan, A., Byrnes, S., Klapperich, C., 2013. Purification of DNA/RNA in a microfluidic device. Microfluid. Diagn.: Methods Protoc., 403–411.

Galambos, P., Forster, F.K., 1998. Micro-fluidic diffusion coefficient measurement. In: Micro Total Analysis Systems' 98. Springer, pp. 189–192.

Hossain, S., Ansari, M.A., Husain, A., Kim, K.-Y., 2010. Analysis and optimization of a micromixer with a modified Tesla structure. Chem. Eng. J. 158, 305–314.

Hsiao, K.-Y., Wu, C.-Y., Huang, Y.-T., 2014. Fluid mixing in a microchannel with longitudinal vortex generators. Chem. Eng. J. 235, 27–36.

Huang, X., Zhu, Y., Zhang, X., Bao, Z., Lei, D.Y., Yu, W., Dai, J., Wang, Y., 2016. Clam-inspired nanoparticle immobilization method using adhesive tape as microchip substrate. Sens. Actuators B Chem. 222, 106–111.

Islam, M., Natu, R., Martinez-Duarte, R., 2015. A study on the limits and advantages of using a desktop cutter plotter to fabricate microfluidic networks. Microfluid Nanofluid 19, 973–985.

Jännig, O., Nguyen, N.-T., 2011. A polymeric high-throughput pressure-driven micromixer using a nanoporous membrane. Microfluid Nanofluid 10, 513–519.

Khosravi Parsa, M., Hormozi, F., Jafari, D., 2014. Mixing enhancement in a passive micromixer with convergent–divergent sinusoidal microchannels and different ratio of amplitude to wave length. Comput. Fluids 105, 82–90.

Kratz, S.R.A., Eilenberger, C., Schuller, P., Bachmann, B., Spitz, S., Ertl, P., Rothbauer, M., 2019. Characterization of four functional biocompatible pressure-sensitive adhesives for rapid prototyping of cell-based lab-on-a-chip and organ-on-a-chip systems. Sci. Rep. 9, 9287.

Lake, M., Narciso, C., Cowdrick, K., Storey, T., Zhang, S., Zartman, J., Hoelzle, D., 2015. Microfluidic Device Design, Fabrication, and Testing Protocols.

Lam, Y.C., Chen, X., Yang, C., 2005. Depthwise averaging approach to cross-stream mixing in a pressure-driven microchannel flow. Microfluid Nanofluid 1, 218–226.

Lee, C.-Y., Wang, W.-T., Liu, C.-C., Fu, L.-M., 2016. Passive mixers in microfluidic systems: a review. Chem. Eng. J. 288, 146–160.

Lim, C.Y., Lam, Y.C., Yang, C., 2010. Mixing enhancement in microfluidic channel with a constriction under periodic electro-osmotic flow. Biomicrofluidics 4, 14101.

Lin, B., 2011. Microfluidics: Technologies and Applications. Springer.

Luong, T.-D., Phan, V.-N., Nguyen, N.-T., 2011. High-throughput micromixers based on acoustic streaming induced by surface acoustic wave. Microfluid. Nanofluid. 10, 619–625.

Nath, P., Maity, T.S., Pettersson, F., Resnick, J., Kunde, Y., Kraus, N., Castano, N., 2014. Polymerase chain reaction compatibility of adhesive transfer tape based microfluidic platforms. Microsyst. Technol. 20, 1187–1193.

Ortega-Casanova, J., 2016. Enhancing mixing at a very low Reynolds number by a heaving square cylinder. J. Fluids Struct. 65, 1–20.

Ortega-Casanova, J., 2017a. Application of CFD on the optimization by response surface methodology of a micromixing unit and its use as a chemical microreactor. Chem. Eng. Process. Process. Intensif. 117, 18–26.

Ortega-Casanova, J., 2017b. CFD study on mixing enhancement in a channel at a low reynolds number by pitching a square cylinder. Comput. Fluids 145, 141–152.

Ortega-Casanova, J., Benitez-Alcaide, P., 2017. Micromixing enhancement by optimizing the geometry of a micromixer by means of response surface methodology: application to chemical microreactors. Micro Nanosyst. 9, 28–38.

Ortega-Casanova, J., Lai, C.H., 2018. CFD study about the effect of using multiple inlets on the efficiency of a micromixer. Assessment of the optimal inlet configuration working as a microreactor. Chem. Eng. Process. Process. Intensif. 125, 163–172.

Park, J.M., Seo, K.D., Kwon, T.H., 2009. A chaotic micromixer using obstruction-pairs. J. Micromech. Microeng. 20, 015023.

Parsa, M.K., Hormozi, F., Jafari, D., 2014. Mixing enhancement in a passive micromixer with convergent–divergent sinusoidal microchannels and different ratio of amplitude to wave length. Comput. Fluids 105, 82–90.

Patsis, G., Petropoulos, A., Kaltsas, G., 2012. Modelling and evaluation of a thermal microfluidic sensor fabricated on plastic substrate. Microsyst. Technol. 18, 359–364.
Sadegh Cheri, M., Latifi, H., Salehi Moghaddam, M., Shahraki, H., 2013. Simulation and experimental investigation of planar micromixers with short-mixing-length. Chem. Eng. J. 234, 247–255.
Salas, A., Ortega-Casanova, J., 2016. Parametric Optimization of a Laminar-Flow Micromixer by CFD., pp. 143–168.
Sivashankar, S., Agambayev, S., Mashraei, Y., Li, E.Q., Thoroddsen, S.T., Salama, K.N., 2016. A "twisted" microfluidic mixer suitable for a wide range of flow rate applications. Biomicrofluidics 10, 034120.
Tóth, E.L., Holczer, E.G., Iván, K., Fürjes, P., 2014. Optimized simulation and validation of particle advection in asymmetric staggered herringbone type micromixers. Micromachines 6, 136–150.
Treise, I., Fortner, N., Shapiro, B., Hightower, A., 2005. Efficient energy based modeling and experimental validation of liquid filling in planar micro-fluidic components and networks. Lab Chip 5, 285–297.
Tretheway, D.C., Meinhart, C.D., 2002. Apparent fluid slip at hydrophobic microchannel walls. Phys. Fluids 14, L9–L12.
Verma, M.S., Tsaloglou, M.-N., Sisley, T., Christodouleas, D., Chen, A., Milette, J., Whitesides, G.M., 2018. Sliding-strip microfluidic device enables ELISA on paper. Biosens. Bioelectron. 99, 77–84.
Wang, Y., Zhe, J., Chung, B.T., Dutta, P., 2008. A rapid magnetic particle driven micromixer. Microfluid. Nanofluid. 4, 375–389.
Xu, B., Wong, T.N., Nguyen, N.-T., Che, Z., Chai, J.C.K., 2010. Thermal mixing of two miscible fluids in a T-shaped microchannel. Biomicrofluidics 4, 044102.
Yang, A.-S., Chuang, F.-C., Chen, C.-K., Lee, M.-H., Chen, S.-W., Su, T.-L., Yang, Y.-C., 2015. A high-performance micromixer using three-dimensional Tesla structures for bio-applications. Chem. Eng. J. 263, 444–451.
Zhang, Y., Hu, Y., Wu, H., 2012. Design and simulation of passive micromixers based on capillary. Microfluid. Nanofluid. 13, 809–818.
Zhenglong, Li, 2019. Communication—electrochemical impedance signature of a non-planar, interdigitated, flow-through, porous, carbon-based microelectrode. J. Electrochem. Society 166, B1669, http://dx.doi.org/10.1149/2.0041916jes.